Bioactive Materials 44 (2025) 116–130

Contents lists available at ScienceDirect

Bioactive Materials

journal homepage: www.keaipublishing.com/en/journals/bioactive-materials

On-demand imidazolidinyl urea-based tissue-like, self-healable, and antibacterial hydrogels for infectious wound care

Qi Wu [a], Krishanu Ghosal [a], Nadine Kana'an [a], Shounak Roy [a], Nagham Rashed [a], Ranabir Majumder [b], Mahitosh Mandal [b], Liang Gao [c], Shady Farah [a,d,*]

[a] The Laboratory for Advanced Functional/Medicinal Polymers & Smart Drug Delivery Technologies, The Wolfson Faculty of Chemical Engineering, Technion-Israel Institute of Technology, Haifa, 3200003, Israel
[b] School of Medical Science and Technology, Indian Institute of Technology Kharagpur, West Bengal, 721302, India
[c] Jinan Key Laboratory of High Performance Industrial Software, Jinan Institute of Supercomputing Technology, Jinan, 250000, China
[d] The Russell Berrie Nanotechnology Institute, Technion-Israel Institute of Technology, Haifa, 3200003, Israel

ARTICLE INFO

Keywords:
Imidazolidinyl urea
Self-healing
Antibacterial hydrogel
Antibiofilm hydrogel
Wound care

ABSTRACT

Bacterial wound infections are a growing challenge in healthcare, posing severe risks like systemic infection, organ failure, and sepsis, with projections predicting over 10 million deaths annually by 2050. Antibacterial hydrogels, with adaptable extracellular matrix-like features, are emerging as promising solutions for treating infectious wounds. However, the antibacterial properties of most of these hydrogels are largely attributed to extrinsic agents, and their mechanisms of action remain poorly understood. Herein we introduce for the first time, modified imidazolidinyl urea (IU) as the polymeric backbone for developing tissue-like antibacterial hydrogels. As-designed hydrogels behave tissue-like mechanical features, outstanding antifreeze behavior, and rapid self-healing capabilities. Molecular dynamics (MD) simulation and density functional theory (DFT) calculation were employed to well-understand the extent of H-bonding and metal-ligand coordination to finetune hydrogels' properties. *In vitro* studies suggest good biocompatibility of hydrogels against mouse fibroblasts & human skin, lung, and red blood cells, with potential wound healing capacity. Additionally, the hydrogels exhibit good 3D printability and remarkable antibacterial activity, attributed to concentration dependent ROS generation, oxidative stress induction, and subsequent disruption of bacterial membrane. On top of that, *in vitro* biofilm studies confirmed that developed hydrogels are effective in preventing biofilm formation. Therefore, these tissue-mimetic hydrogels present a promising and effective platform for accelerating wound healing while simultaneously controlling bacterial infections, offering hope for the future of wound care.

1. Introduction

Since the 21st century, bacterial infections have become a formidable challenge in healthcare [1], with surgical site infections (SSIs) and urinary tract infections (UTIs) representing approximately 55 % of incidence among nosocomial infections as reported in 2002 [2]. It is estimated that by 2050, humankind will face a staggering toll, with over 10 million annual deaths attributed to bacterial infections, surpassing all other causes of mortality-including cancer [3]. Bacterial wound infections caused by pathogenic bacteria prolong the healing process and pose significant risks of systemic infection, organ failure, and sepsis, underscoring an urgent need for effective interventions [4]. Although the discovery of antibiotics initially curbed the advancement of bacterial infections, drug abuse has led to antibiotic-resistant strains among pathogenic bacteria [5]. To counter such challenges, varieties of innovative materials with antimicrobial properties have been developed, such as nanomaterials [6,7], foam [8,9], nanofibers [10,11], and hydrogels [12–15]. Among these agents, hydrogels with tunable tissue-like features, remarkable absorption capability, biodegradability, biocompatibility [14,16], and extracellular matrix (ECM)-like porous structure have emerged as the most promising candidates for bacterial-infected wound treatments. However, the most reported

Peer review under responsibility of KeAi Communications Co., Ltd.
* Corresponding author. The Laboratory for Advanced Functional/Medicinal Polymers & Smart Drug Delivery Technologies, The Wolfson Faculty of Chemical Engineering, Technion-Israel Institute of Technology, Haifa, 3200003, Israel.
E-mail address: sfarah@technion.ac.il (S. Farah).

https://doi.org/10.1016/j.bioactmat.2024.10.003
Received 21 February 2024; Received in revised form 15 September 2024; Accepted 1 October 2024
2452-199X/© 2024 The Authors. Publishing services by Elsevier B.V. on behalf of KeAi Communications Co. Ltd. This is an open access article under the CC BY-NC-ND license (http://creativecommons.org/licenses/by-nc-nd/4.0/).

antibacterial hydrogels rely on incorporating additional active compounds, such as drugs or nanomaterials, instead of inherent antibacterial characteristics [17–19]. These investigations have not paid enough attention to the origins of antibacterial activities and how they lead to bacterial death.

In general, antibacterial agents inactivate bacteria mainly by damaging their membranes, preventing the production of cell walls, targeting intercellular molecules, and by immunomodulation [20]. Many cationic polymers kill bacteria through electrostatic interaction, followed by hydrophobic insertion into lipid tails and subsequent membrane lysis [21–23]. Moreover, they can inhibit the production of cell walls by targeting lipid II [24,25], a crucial precursor in the biosynthesis of peptidoglycan layers, ultimately leading to disruption of bacterial growth. When targeting intercellular molecules, specific antibacterial agents can overcome the barriers posed by the outer membrane and cytoplasmic membrane [26,27]. These agents may accumulate within the cytosol, strongly interact with DNA, inhibit cell division, condense bacterial chromosomes, and inhibit nucleic acid synthesis to disrupt critical intracellular processes. For immunomodulatory mechanisms, antibacterial agents effectively recruit immune cells like neutrophils, macrophages, and T cells to the infection sites, thereby promoting bacterial clearance. Moreover, they can also enhance neutrophil function, suppress the release of pro-inflammatory cytokines, facilitate the induction of anti-inflammatory cytokines, and promote phagocytosis [28,29]. Hence, a thorough investigation into deciphering the mechanism provides a deeper understanding of the intricate relationship between their structure, properties, and efficacy against various microbial species, guiding more effective antimicrobial materials' development.

In addition to exploring antibacterial mechanism studies, another challenge is designing innovative multifunctional materials. Urea and its derivatives play a significant role in medicinal applications, such as modulating drug potency, selectivity, and pivotal interactions with drug targets [30]. In recent years, several urea derivatives have emerged as effective antimicrobial agents, offering promising solutions to fight against microbial infections [31–33]. Imidazolidinyl urea (IU) is an antimicrobial preservative used to formulate pharmaceutical products, cosmetics, and household detergents [34]. Recently, with increasing attention to preservatives, more research has been devoted to the IU molecule. For example, Wang et al. prepared the IU-grafted reverse osmosis membrane, in which IU acted as both the antimicrobial agent and the precursor of N-halamine. A reversible transition between N-Cl and N-H groups happened during sterilizing microbial cells and the chlorination process [35]. Apart from chemical and biological functionalities, rich H-bonding donors and receptors from IU could promote the formation of multiple hydrogen bonds. For example, Cheng's group has reported H-bonding reinforced biocompatible hydrogels and observed that the introduction of IU contributed to superior mechanical properties, self-healing and shape memory abilities, and degradability [36–40]. Moreover, IU-based hydrogels were utilized as tannic acid-loading carriers for diabetic wound healing and infectious skin treatments [41], as tannic acid/kartogenin-loading scaffold for *in vivo* cartilage regeneration [40]. In our recent work, we designed IU-based photoresins for high-resolution 3D printing, and the printed objects exhibited potent antimicrobial activity [42]. Overall, all these studies exploited its promising potential in both structural superiorities and functionalities. However, in most of these studies, IU was utilized either as a small molecule, an additive or as a part of a structural backbone without evaluating its biological performance and intrinsic antibacterial mechanism of action in detail.

In this study, for the first time, we incorporated a modified IU molecule as the polymers' backbone and explored its inherent biological properties, especially antibacterial performance and its mechanisms. By integrating both structural and functional advantages, we have developed several IU-based tissue-like hydrogels through free radical polymerization under mild conditions. Dynamic metal-ligand coordination was introduced into the system to tune mechanical properties, such as strength, modulus, and fatigue. Tensile/compression tests and density functional theory (DFT) calculation were combined for formulation optimization. In addition to structural and morphological characterization (NMR and SEM), FTIR and molecular dynamics (MD) simulation were utilized for hydrogen bonding investigation, followed by antifreeze, rheological, and self-healing behavior studies. Then, we evaluated *in vitro* cytocompatibility of designed hydrogels against three distinct cell lines NIH/3T3 mouse fibroblasts, BEAS-2B human lung epithelial cells, and HaCaT human keratinocytes, assessed hemocompatibility against human red blood cells, and conducted *in vitro* wound healing assay. Furthermore, we studied their antibacterial performance against both gram-negative *Escherichia coli* (*E. coli*) and gram-positive *Bacillus subtilis* (*B. subtilis*); followed by an in-depth investigation to unravel the intrinsic antibacterial mechanism through an amalgamation of both experimental and theoretical (MD simulation) strategies. Lastly, we studied their capabilities to prevent biofilm formation.

2. Results and discussion

2.1. Synthesis and mechanical study

We synthesized acylated IU monomer under mild conditions from commercial cosmetic preservative imidazolidinyl urea (IU, Scheme S1); the structure was confirmed by FTIR (Fig. S1), ^{1}H NMR (Figs. S2 and S3), and ^{13}C NMR (Fig. S4). In Fig. S1, new peaks at 862 and 3066 cm^{-1} correspond to the C=C bending and C-H stretching of C=C, respectively, indicating the successful incorporation of the acrylate group within the IU structure. Furthermore, new peaks at 5.86, 6.01, and 6.27 ppm from ^{1}H NMR (Figs. S2 and S3) indicate the presence of acrylate protons. On the other hand, two new peaks are observed at 129 and 131 ppm in ^{13}C NMR (Fig. S4) belonging to acrylate carbons, which strongly confirms the successful synthesis of IU monomer. Then, IU-based hydrogels were prepared by copolymerizing IU monomer and methacrylamide (MAA), via free radical polymerization using ammonium persulfate (APS) as initiator and N,N,N′,N′-tetramethylethylenediamine (TEMED) as a catalyst in deionized water at 37 °C (Fig. 1a, Fig. S5). The optimization of formulations and conditions was based on the mechanical (tensile and compression) tests (Fig. S6). After optimization, at a molar ratio of 1:2.5 between IU monomer and MAA and 50 % of monomer concentration, we obtained a soft and highly stretchable hydrogel PMIU (Fig. S7). The excellent stretchability is attributed to the enriched hydrogen bonding facilitated by the imidazolidinyl urea structure [37,41]. However, it has poor physical stability and is soluble in water, which demands further improvement in its mechanical properties. For emerging applications such as artificial tissues and wound healing dressings, materials must maintain stability and durability under prolonged mechanical stress, resisting cyclic fatigue damage or fracture [43]. In this regard, we opted for dynamic metal-ligand coordination instead of covalent crosslinking to enhance hydrogel's stability and mechanical strength, with the accessional value of reversible response under damage, such as self-healing capability. Therefore, we introduced a low ratio of vinyl imidazole (VI) and Ni^{2+}/Zn^{2+} salts into the PMIU system; the imidazole moiety as an integral component of specific amino acids found in various peptides [44], which can coordinate with different metals for constructing and tuning metallogels' performance and behavior [45,46]. From the optimization, there was no significant improvement in hydrogels' mechanical performance by introducing a low amount of vinyl imidazole, only if metal ions Ni^{2+}/Zn^{2+} were present to trigger metal-ligand coordination. With the increase of vinyl imidazole and related metal ions, the mechanical properties of synthesized hydrogels increased, and the materials became stiffer. Whenever the molar ratio of vinyl imidazole and IU monomer is above 0.5, the precursor solution will be crosslinked quickly after initiation of polymerization. This sudden increase in viscosity is attributed to the strong metal-ligand

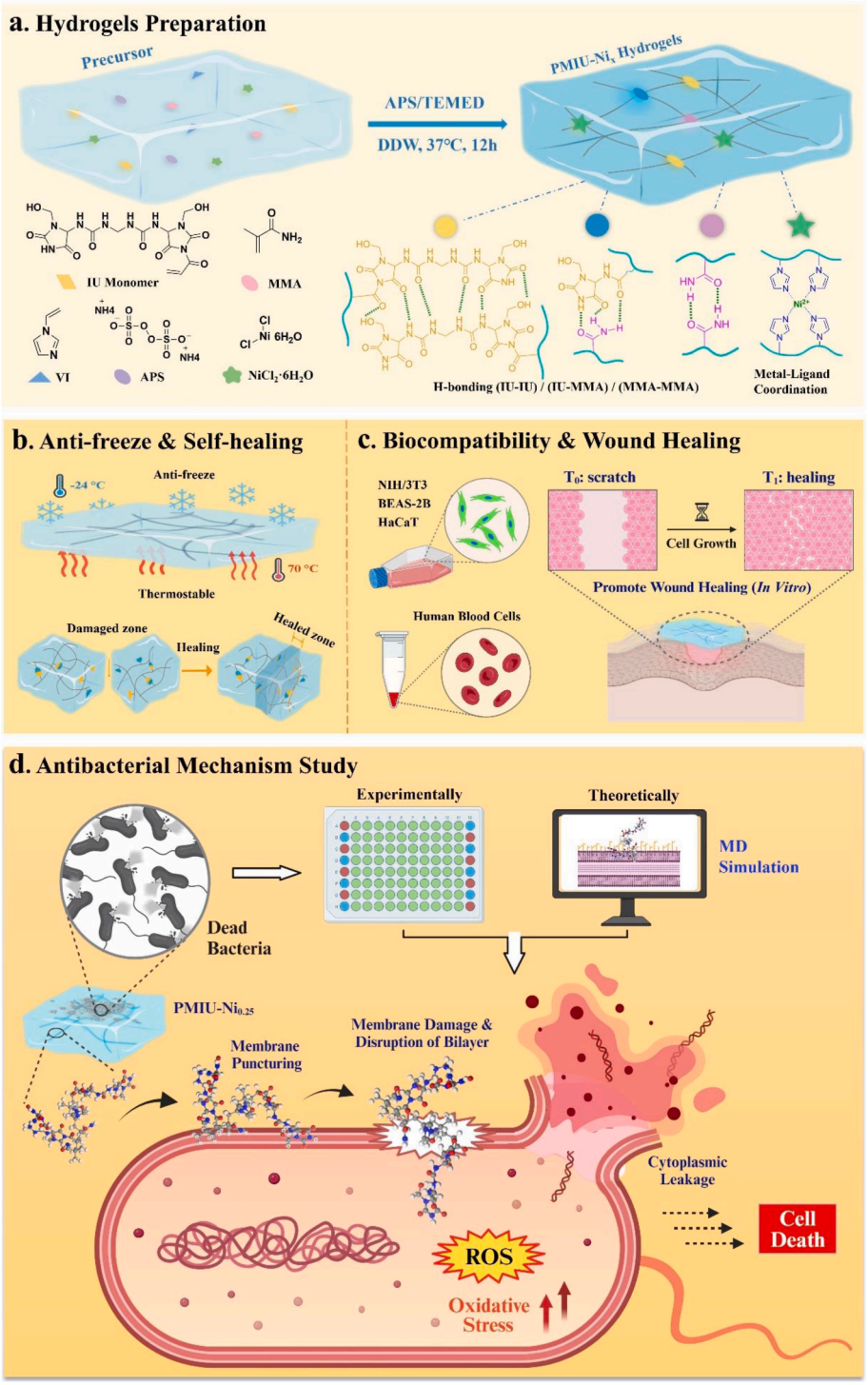

Fig. 1. Schematic illustration of this work. a) Hydrogels preparation; b) Anti-freeze and self-healing; c) Biocompatibility and wound healing; d) Antibacterial mechanism study.

coordination and H-bonding interactions that took place simultaneously. However, we are aiming to design tissue-like hydrogels for biomedical applications, therefore we chose the molar ratio between IU monomer and vinyl imidazole of 4:1 to balance the mechanical performance and flexibility.

Here, several metal-ligand reinforced hydrogels PMIU-Ni_x and PMIU-Zn_y were synthesized, where x (0.125, 0.25 and 0.5) and y (0.125, 0.25 and 0.5) stand for the ratios between Ni^{2+}/Zn^{2+} and VI, respectively. Fig. 2a and c represent tensile and compression stress-strain curves for all IU-based hydrogels, respectively. Polymethacrylamide (PMAA) hydrogel was used as a control. For hydrogels PMIU-Zn_y, mechanical properties increased with the increase of the Zn^{2+} ratio. While for PMIU-Ni_x, PMIU-$Ni_{0.25}$ shows the best balance between the tensile strength of 214.71 ± 3.94 kPa and strain of 477.07 ± 34.64 % (Fig. S8), with the elastic modulus of 471.19 ± 17.52 kPa and toughness of 623.665 ± 84.82 kJ/m^3 (Fig. 2b). Similarly, for the compression tests, PMIU-$Ni_{0.25}$ also exhibits remarkable compressive strength (447.26 ± 28.26 kPa), strain (86.32 ± 3.91 %), stiffness (77.34 ± 4.83 kPa), and toughness (69.16 ± 4.25 kJ/m^3), as shown in Figs. S8 and 2d. In particular, the hydrogel PMIU-$Ni_{0.125}$ shows better mechanical performance than

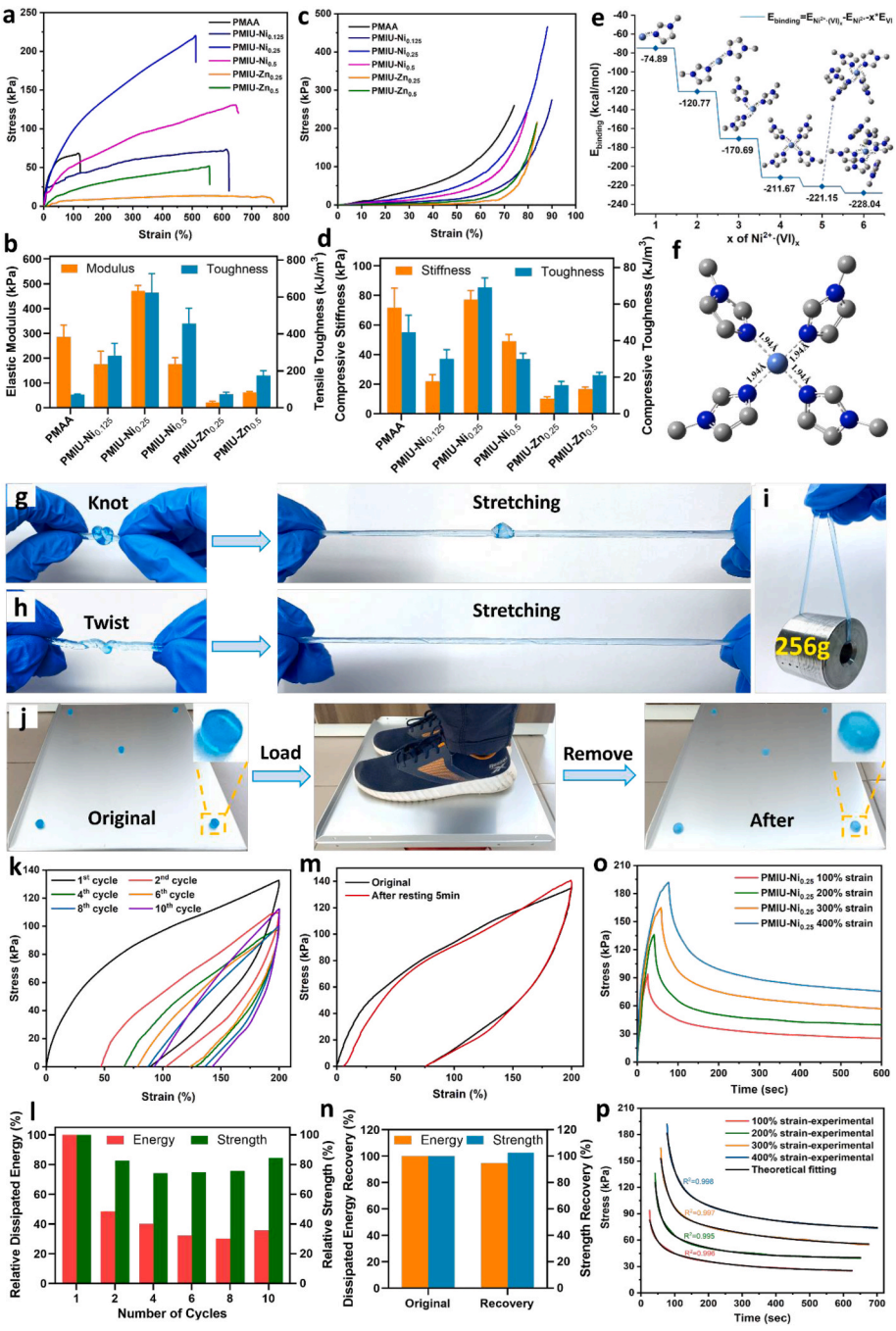

Fig. 2. Optimization and mechanical study of hydrogels. a) Tensile stress-strain curves at a strain rate of 40 mm/min; b) Elastic modulus and tensile toughness. c) Compression stress-strain curves at compressive rate of 1 mm/min; d) Compressive stiffness and toughness. e) Density functional theory calculation of binding energy between Ni^{2+} and different number imidazole ligands; f) DFT snapshots of optimized structure between Ni^{2+} and imidazole ligand ratio of 1:4. Photographs of hydrogel PMIU-$Ni_{0.25}$, g) knot and knot stretch; h) twist and twist stretch; i) 1 g hydrogel lifting 256 g weight; j) five hydrogel cylinders taking a person (60 kg) without apparent collapse. Tensile cyclic loading-unloading study of PMIU-$Ni_{0.25}$ at 200 % strain, k) ten successive fatigue cycles; l) relative dissipated energy and strength of ten fatigue cycles at 200 % strain; m) original and after rest for 5 min at 200 % strain; n) dissipated energy and strength recovery after 5 min rest at 200 % strain. Stress relaxation study of hydrogel PMIU-$Ni_{0.25}$, o) experimental curves at different strains; p) fitting curves by combing two viscoelastic (Maxwell) and one elastic (Viogt) elements in parallel.

PMIU-$Zn_{0.5}$, indicating that more efficient chelation occurred between Ni^{2+} and the imidazole group than Zn^{2+}. To quantitatively assess the metal-ligand coordination in this system, we calculated the binding energy between Ni^{2+} and different numbers of imidazole ligands (1–6) using density functional theory (DFT) calculation (S1.7, ESI). Interestingly, the optimized structures in Fig. 2e, one ligand of $Ni^{2+}\cdot(VI)_5$ and two ligands of $Ni^{2+}\cdot(VI)_6$ dissociated from Ni^{2+}, respectively. The binding energies of both structures are approximate to $Ni^{2+}\cdot(VI)_4$. Meanwhile, from Table S1, both optimized $Ni^{2+}\cdot(VI)_5$ and $Ni^{2+}\cdot(VI)_6$ structures have 4 equal N-Ni^{2+} bonds with bond length around 1.94 Å, same as $Ni^{2+}\cdot(VI)_4$ (Fig. 2f). While $Ni^{2+}\cdot(VI)_5$ has another different N-Ni^{2+} bond with a length of 3.62 Å, and $Ni^{2+}\cdot(VI)_6$ has two different bonds with lengths of 2.93 and 3.53 Å, proved that the dissociation between Ni^{2+} and part of imidazole ligands takes place. Concluding the binding energy and bond length distributions of these three structures, the ratio of 1:4 between Ni^{2+} and imidazole ligand resulted in the

optimum coordination. This quantitative calculation coincides well with tensile/compression results, that the hydrogel PMIU-$Ni_{0.25}$ exhibits pioneering mechanical performance. Overall, the designed hydrogels achieved a comprehensive improvement in stretchability and strength compared to PMAA hydrogel, by collaborating rich hydrogen bond interactions along with dynamic reversible metal-ligand coordination [47,48]. According to mechanical properties, we featured hydrogels PMIU (as a reference) and PMIU-$Ni_{0.25}$ for further studies. Figs. S9, 2g, 2h, and 2i illustrate the robust mechanical properties of PMIU-$Ni_{0.25}$ hydrogel. A hydrogel ribbon (~2 mm, 1 g) was stretched in normal, knotted, and twisted conditions and still was able to withstand the high strain. In addition, it could lift ~256 g of weight without rupture, indicating superior mechanical strength. Also, Fig. S10 clearly shows the tissue-like flexibility of PMIU-$Ni_{0.25}$ hydrogel, which could repeatedly bend on the finger and elbow between 90 and 180°. Moreover, five hydrogel cylinders could take a person (~60 kg) without evident collapse, as shown in Fig. 2j. This could mainly attributed to diverse physical interactions of H-bonding, especially metal-ligand coordination, as sacrificial bonds that strengthen mechanical properties, including toughness. Toughness would help to dissipate energy during the sample deformation but possibly cause fatigue, implying the degradation of hydrogel properties [49].

Inspired by this observation and hypothesis, we investigated the fatigue of hydrogel PMIU-$Ni_{0.25}$ by cyclic tensile loads. From Fig. S11, dissipated energy (hysteresis area between loading and unloading curves) increases with strain percentages, around 65–80 % of the total work. When stress is applied, energy will be dissipated due to the breakage of sacrificial bonds; the broken inter-chain reversible bonds will change the network topologies of hydrogels, where the network topologies will significantly affect the fatigue behavior. Lin et al. introduced partially crystalline structures in polyvinyl alcohol hydrogels and achieved a superior fatigue threshold exceeding 1000 J/m^2 [43]. The required energy per unit area for fracturing fatigue cracks in highly ordered networks was much higher than in a single layer of polymer chains. Here, ten loading-unloading cycles were proceeded with PMIU-$Ni_{0.25}$ to quantify the cyclic fatigue damage at 200 % strain. From Fig. 2k and l, a substantial hysteresis loop is observed in the 2nd cycle with 50 % dissipated energy and 20 % strength drop; the cyclically applied loads without rest caused ongoing damage to sacrificial bonds. Interestingly, after 6 cycles, both dissipated energy and strength started to increase, possibly due to the partial rejoint of the broken sacrificial bonds, which helped to rebuild the disordered networks. Also, fatigue crack-resistant effects in different directions of 3D networks amplify the antifatigue behavior [46,50]. Inspired by this interesting observation, a second loading-unloading cycle was conducted on the first cycle sample but after a 5-min rest. As expected, almost no hysteresis of the loading-unloading loop is observed (Fig. 2m and n), and the dissipated energy and strength recovery to 95 % and 103 % of the original hydrogel, respectively. Meanwhile, fatigue of PMIU-$Ni_{0.25}$ was also studied by cyclic compression loads at 60 % strain; similar conclusions as tensile loads vide supra (Fig. S12). In sum, the above results reveal that the hydrogel PMIU-$Ni_{0.25}$ possesses robust fatigue resistance properties under multiple cycles of loads and extraordinary recovery characteristics.

Fatigue correlates with rheology, a liquid-like hydrogel will relax to zero stress under a prolonged static stretch without increasing static and cyclic fatigue threshold. Meanwhile, a solid-like hydrogel relaxes to finite stress (nonzero) and with an increase in static fatigue threshold [49]. Stress relaxation seeks to understand the mechanism of hydrogel fracture and fatigue differently. In this work, we studied the stress relaxation behavior of PMIU-$Ni_{0.25}$ at different strains. From Fig. 2o, similar trends of stress evolution versus time are observed from different strain curves: a rapid drop followed by a nonzero plateau, indicating the solid-like behavior of the hydrogel. Like uniaxial tensile stretch, stress comes from sacrificial bonds and drives the chain segment orientation during loading. During relaxation, a dramatic stress reduction is ascribed to the breakage of sacrificial bonds, which could weaken inter-chain interactions and cause the relaxation of chain segment orientation. Although efficient recovery happens, rebuilt networks are relaxed, without contributing to strain energy and chain order [51]. Constant stress at a nonzero plateau relies on the elasticity of the inherent polymer chains and entangled networks [52]. To concretely describe the viscoelastic behavior, the stress relaxation data was fitted by the model combining two viscoelastic (Maxwell) and one elastic (Viogt) elements in parallel (Fig. S13). From Fig. 2p, the theoretically fitted curves of PMIU-$Ni_{0.25}$ at 100 %, 200 %, 300 %, and 400 % strains highly match the experimental data, with squares of the correlation coefficient exceeding 0.995.

Hence, the stress relaxation behavior is described as Equation (1):

$$\sigma_t = \sigma_1 + \sigma_2 + \sigma_3 = E_1\varepsilon_0 \exp(-(t-t_0)/\tau_1) + E_2\varepsilon_0 \exp(-(t-t_0)/\tau_2) + E_3\varepsilon_0 \quad (1)$$

Where σ_t is the total stress, σ_i and E_i are the stress and elastic modulus of each unit, respectively. ε_0 is the constant initial strain, t_0 is the initial relaxation time. τ_i is the response of the one-dimensional Maxwell element, represented by the ratio of viscosity η_i to elastic modulus E_i, $\tau_i = \eta_i/E_i$.

Meanwhile, the relaxation modulus E_r can be calculated by Equation (2):

$$E_r = \sigma_t/\varepsilon_0 = E_1 \exp(-(t-t_0)/\tau_1) + E_2 \exp(-(t-t_0)/\tau_2) + E_3 \quad (2)$$

All characteristic parameters related to Equations (1) and (2) are shown in Table S2.

2.2. Physical study

The microstructure of IU-based hydrogels was analyzed by a high-resolution scanning electron microscope (HR-SEM). Fig. 3a and b shows that both hydrogels exhibit three-dimensional (3D) networks, while a denser and more orderly packed network is observed at the PMIU-$Ni_{0.25}$ network. Average pore size distribution curves fitted by the Gaussian function show a more uniform microstructure with homogenous pores in PMIU-$Ni_{0.25}$ compared to PMIU. The dynamic covalent bonds between Ni^{2+} and imidazole moiety are the dominant contribution for driving the network organization, instead of physical cross-linking through polymer chain entanglement and multiple H-bonding interactions [53,54]. Next, FTIR was employed for hydrogel structural characterization, as shown in Figs. S14 and S15, the spectrums evidence the successful synthesis of hydrogels. To further investigate the H-bonding interactions, we analyzed the FTIR spectrums of hydrogels PMIU and PMIU-$Ni_{0.25}$ from 1740 to 1500 cm^{-1} and fitted it with the Gaussian function, as shown in Fig. 3c and d. For both hydrogels, fitted curves closely match the experimental curves, and 7 separate peaks are obtained; where peaks I, II, III, IV, and V are related to H-bonded C=O, free C=O, H-bonded C=O, H-bonded C=O, and free amide, respectively. In addition, peaks VI and VII for PMIU indicate the existence of H-bonded N-H and free N-H. For PMIU-$Ni_{0.25}$, peak VI belongs to a free N-H bending, while peak VII belongs to an H-bonded N-H [55]. Furthermore, we utilized Molecular Dynamics (MD) simulation to further analyze hydrogen bonds composition. Three representative cubic boxes were constructed to simulate the experimental hydrogel systems and optimized by a Forcite module with a COMPASS II force field. Due to the lack of Ni^{2+} ion in this force field, we built a PMIU-$Zn_{0.5}$ hydrogel system instead of PMIU-$Ni_{0.25}$ (S1.8, ESI). Fig. 3e–S16, and 3g represent the equilibrium state of PMIU, PMIU-VI, and PMIU-$Zn_{0.5}$, respectively. Meanwhile, snapshots of optimized structures shown in Fig. 3f and h intuitively exhibit the H-bonding interactions between different moieties. After equilibrium, different types and numbers of hydrogen bonds were counted and analyzed, as shown in Fig. 3i. In all systems, more than 70 % of H-bonds comes from inter IU monomers, IU monomer and water molecule, IU monomer and MMA, proving the

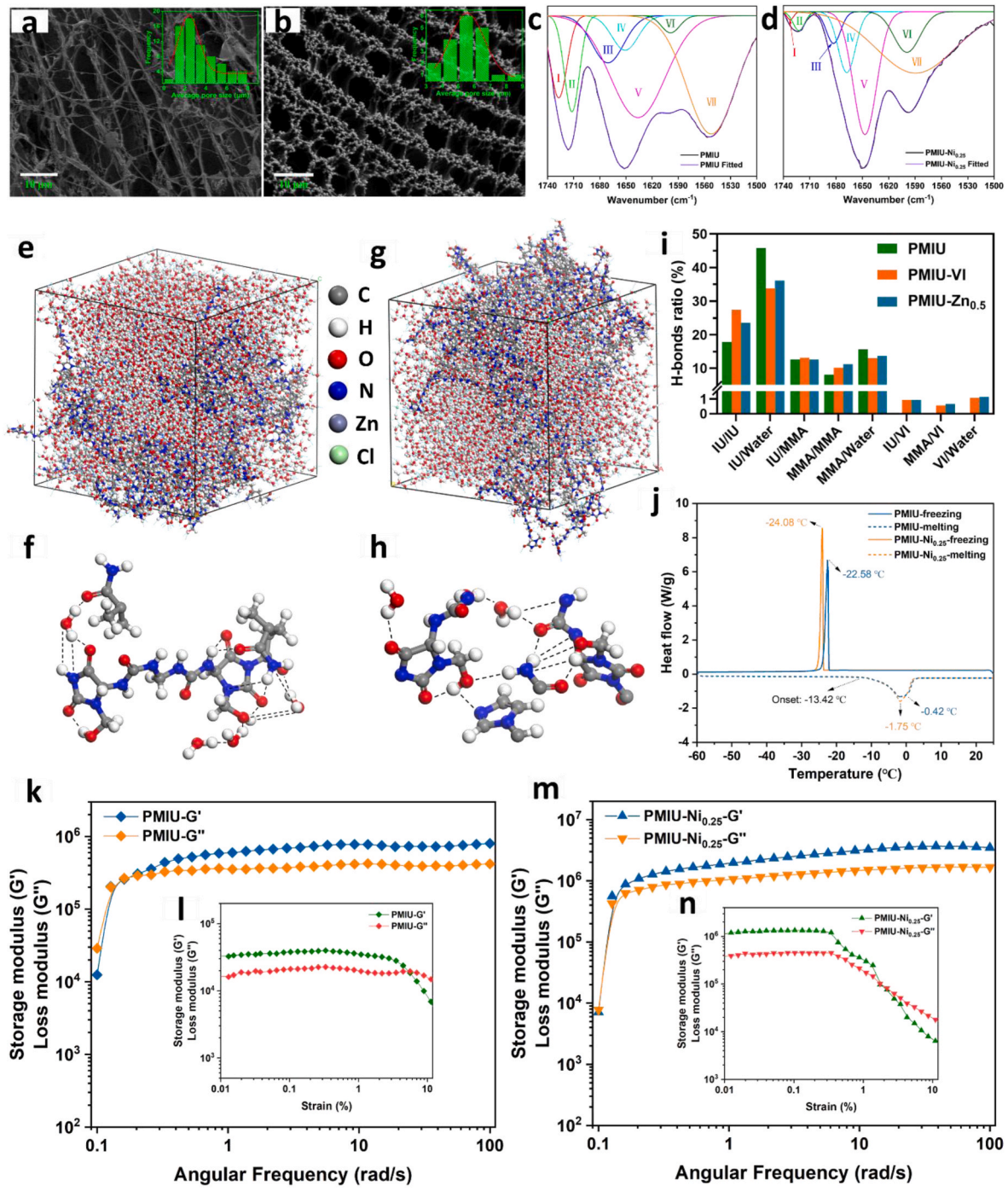

Fig. 3. Physical study of hydrogels. SEM images of freeze-dried hydrogels, a) PMIU; b) PMIU-$Ni_{0.25}$. Gaussian fitting of hydrogels FTIR curves (1740-1500 cm^{-1}) for hydrogen bonding study, c) PMIU; d) PMIU-$Ni_{0.25}$. MD simulation of hydrogels system for H-bonding study, e) equilibrium state of hydrogel PMIU system; g) equilibrium state of hydrogel PMIU-$Zn_{0.5}$. MD snapshots of the optimized structure showing H-bonding interactions, f) PMIU system; h) PMIU-$Zn_{0.5}$ system. i) Comparison of hydrogen bond distribution within hydrogels PMIU, PMIU-VI, and PMIU-$Zn_{0.5}$. j) DSC curves of hydrogels PMIU and PMIU-$Ni_{0.25}$ for anti-freeze study. Frequency sweep at 0.1 % strain of, k) PMIU; m) PMIU-$Ni_{0.25}$. Strain sweep at 1 Hz frequency of, l) PMIU; n) PMIU-$Ni_{0.25}$.

dominant H-bonds contribution from imidazolidinyl urea as expected. And the H-bonds distributions between PMIU and PMIU-$Zn_{0.5}$ systems further match the experimental results, that the hydrogels PMIU-Ni_x and PMIU-Zn_y sustained surprised flexibility and stretchability after metal-ligand chelation, with substantial improvement in mechanical performance.

Besides H-bonding analysis, thermostability and anti-freeze properties of synthesized hydrogels were also evaluated using Thermogravimetric Analysis (TGA) and Differential Scanning Calorimetry (DSC). For biomaterials and devices, extraordinary behaviors under extreme environmental conditions are indispensable to maintain their mechanical stability, conductivity, and other functionalities [56]. The TGA results from Fig. S17 prove the superior water retention capacity and thermal stability of hydrogels at high temperatures. Step I indicates the moisture loss; step II (after 220 °C) is mainly related to the decomposition of the imidazolidinyl urea structure and followed by the decomposition of polymethacrylamide (step III). Fig. 3j represents DSC curves (cooling from 25 °C to −60 °C and then warming to 25 °C) of PMIU and

PMIU-$Ni_{0.25}$ hydrogels; the crystallization/freezing peaks observed at −22.58 and −24.08 °C demonstrating their advanced freeze-tolerant performance to maintain physical performance under extreme cold environment. The mechanisms of antifreeze behavior are mainly H-bonding, structure of components, and chelation effects. Firstly, rich hydrogen bonds between water molecules and polymer structures significantly enhanced hydrogels' moisture-holding capability and freeze tolerance. Meanwhile, introducing hydrophobic moieties (methyl groups) and urea structures into hydrogels could lower the freezing point [57]; the hydrophobic aggregates confined the growth of ice nuclei to proceed with crystallization [58], coincident conclusion as Janus effect of antifreeze proteins (AFPs) that hydrophobic ice-binding face of

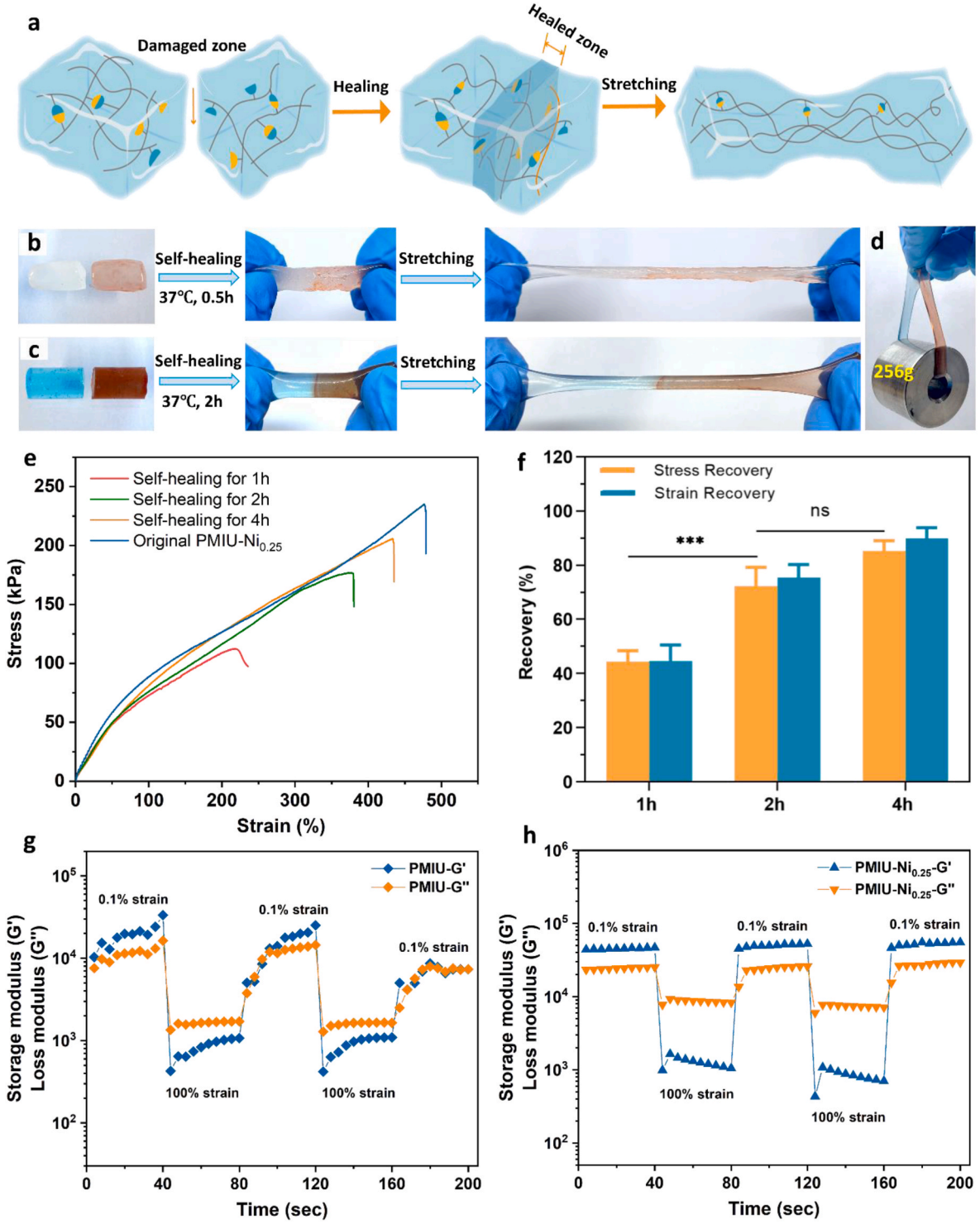

Fig. 4. Self-healing study of hydrogels. a) Schematic diagram of self-healing and stretching process. Photographs of hydrogels self-healing, b) PMIU cutting, healing, and stretching; c) PMIU-$Ni_{0.25}$ cutting, healing, and stretching; d) self-healed hydrogel PMIU-$Ni_{0.25}$ lifting 256 g weight. Mechanical study of self-healed hydrogel PMIU-$Ni_{0.25}$ after 1h, 2h, and 4h, e) tensile stress-strain curves; f) stress and strain recovery. Thixotropic study of hydrogels with step-strain sweep of low strain (0.1 %, 40 s) and high strain (100 %, 40 s), g) PMIU; h) PMIU-$Ni_{0.25}$. Statistical analysis: two-way ANOVA; *, **, ***, and **** were considered for p values < 0.05, <0.01, <0.001, and <0.0001, respectively ($n = 3$).

AFPs inhibit ice formation [59]. Notably, from Fig. 3j, the crystallization of PMIU-$Ni_{0.25}$ happens 1.5° lower than PMIU, likely due to the freezing point depression effect of inorganic salt $NiCl_2$ [60], and denser microstructure (less distance) after chelation, which affects the hydrophobic inhibition efficacy of ice growth [61].

Lastly, to quantitatively assess the flow/deformation of synthesized hydrogels, the rheological properties, especially viscoelastic behavior, were investigated using an oscillatory rheometer. Most hydrogels are non-Newtonian liquids with shear-thinning behavior, where the viscosity decreases as the shear rate increases [62]. As shown in Fig. S18, a higher zero-shear viscosity of PMIU-$Ni_{0.25}$ compared to PMIU is observed, which is due to the higher toughness of PMIU-$Ni_{0.25}$. At the same time, PMIU shows better viscosity maintenance during shear thinning, where its flexible network contributed to less viscosity drop. In addition, temperature sweep results in Fig. S19 indicate favorable thermal stability of both PMIU-$Ni_{0.25}$ and PMIU, consistent with TGA analysis data. Viscoelastic materials generally show viscous and elastic behavior during deformation, while purely elastic materials do without energy dissipation. Storage modulus G′ represents stored deformation energy (i.e., stiffness), and loss modulus G″ reflects dissipated energy (i.e., flow) are defined to describe materials' viscoelastic behavior during the shear process [63]. In this work, we conducted oscillatory strain sweep tests on hydrogels at a frequency of 1 Hz to the abstract linear viscoelastic region (Fig. 3l and n). According to the results, a strain of 0.1 % was opted for frequency sweep experiments. In Fig. 3k and m, PMIU-$Ni_{0.25}$ shows more elastic/solid-like behavior while PMIU shifted from viscous to elastic behavior with the increase of frequency. Additionally, the moduli of PMIU-$Ni_{0.25}$ are much higher than PMIU, corresponding to more preceding stiffness and strength contributed by metal-ligand coordination and lower flexibility, as shown in the mechanical study.

2.3. Self-healing study

In general, self-healing hydrogels can be used as wound-healing dressings, artificial tissues, biosensors, and actuators [64,65]. A schematic diagram of hydrogel's self-healing and stretching processes is shown in Fig. 4a, with both damaged and healed zones, illustrating the rejoining of sacrificial bonds after damage and their behavior while stretching. This healed zone is the weak point of the sample, challenging the healing capacity of sacrificial bonds for energy dissipation, to resist the growth of cracks or fractures instead of a homogenous recovered fatigue system. To evaluate the self-healing performance of designed hydrogels, we cut both prepared PMIU and PMIU-$Ni_{0.25}$ into two segments (one colored by Congo red), and attached them together for healing, as shown in Fig. 4b and c. For soft hydrogel PMIU, the self-healing happened at body temperature within a half hour. While for stiffer hydrogel PMIU-$Ni_{0.25}$, we tracked the self-healing process after 1h, 2h, and 4h, respectively. As expected, both healed hydrogels exhibit excellent stretchability. Also, after 2h healing, PMIU-$Ni_{0.25}$ could still lift 256 g of weights (Fig. 4d). Then, the self-healing efficiency of PMIU-$Ni_{0.25}$ at different time points was checked by mechanical tensile test. Fig. 4f shows the strength and stretchability recovery percentage calculated from stress-strain curves (Fig. 4e). Compared to the original hydrogel, after 2h, the stress of PMIU-$Ni_{0.25}$ can recover to around 72.28 %, and strain can return to 75.43 %; while after 4h, stress and strain can recover to about 85.3 % and 89.82 %, respectively. This result strongly indicates the fast and excellent self-healing performance. In addition to that, we performed step-strain sweep (thixotropic) experiments to assess the intrinsic self-healing capacity. Synthesized hydrogels were tested under the alternative applied strain of 0.1 % (linear viscoelastic region) and 100 % (non-linear region) at a constant frequency of 1Hz, 40 s for each application. Fig. 4g and h shows that storage and loss moduli at the strain of 0.1 % decreased and reversed instantly when 100 % of the strain was applied. The deformation of hydrogel networks happens within a nonlinear regime, in which modulus is the function of strain amplitude. Then, the modulus effectively recovered toward the original state upon returning to 0.1 % of the strain, indicating reattachment of sacrificial bonds, which leads to the network reconstruction. This alternative modulus changes behavior under step-strain reveals shear-induced reversible gel-sol transition of synthesized hydrogels. In this system, the self-healing mechanism mainly involves H-bonding interactions, reversible metal-ligand coordination, and thermal effects. During healing, the broken H-bonds between molecules and water will reassociate at damaged zone; the recovered H-bonding will reconstruct the inter-chain interactions for crosslinking. For PMIU-$Ni_{0.25}$, dynamic Ni^{2+}-imidazole coordination happens in a short time except for H-bonding interactions; the rebuilt sacrificial bonds will strengthen the hydrogel networks, heal the damage, and efficiently recover its mechanical performance. As observed in Fig. 4g and h, compared to slight moduli loss of PMIU, almost 100 % moduli of PMIU-$Ni_{0.25}$ was recovered after two cycles, which is mainly due to the synergistic effect of dual crosslinking. Lastly, thermal effects from external heating will accelerate the polymer chains' movement and promote reassociation and crosslinking.

2.4. In vitro biocompatibility and In vitro wound healing

Assessing biocompatibility is essential to identify potential adverse effects of newly developed materials intended for biomedical applications [66]. In this study, Alamar blue assay [67] was used to evaluate the cytotoxicity of synthesized hydrogels against three distinct cell lines, NIH/3T3 mouse fibroblasts, BEAS-2B human lung epithelial cells, and HaCaT human keratinocytes for 7 days. Figs. S20 and 5a illustrate the cell viability in PMIU (soluble) and PMIU-$Ni_{0.25}$ (leach liquor) conditioned media, treated against control. No significant cytotoxic effects were observed for all except the BEAS-2B cells with PMIU. After one day, the cells treated with conditioned media of PMIU-$Ni_{0.25}$ didn't affect the normal metabolic activity cells as supported by excellent cell attachment similar to TCPS (control), with no statistically significant difference. Substantial cell growth is observed after 3 and 7 days, respectively, indicating that the leach liquor from PMIU-$Ni_{0.25}$ is non-cytotoxic in the long term. Moreover, to gain further significant insights into cellular activity, we performed live-dead semiquantitative fluorescence imaging (Fig. 5c-e); and examined cellular morphology (Fig. 5f-h) for all three cell types treated with standard media and conditioned media of PMIU-$Ni_{0.25}$. The nucleus was stained with DAPI, and the actin filaments of cells were stained with Alexa fluor phalloidin. For days 1, 3, and 7, all the cells display a healthy and evenly distributed pattern with no significant difference in control. The live-dead and cellular morphology demonstrate the effective communication between neighboring cells through filopodial protrusions, supporting the cell viability data and proving the non-cytotoxic nature of the leach liquor from PMIU-$Ni_{0.25}$. Besides cytotoxicity, the blood compatibility of synthesized hydrogels was studied via hemolysis assay on fresh human blood. For the hemolysis study, deionized water was used as positive control, and physical saline was used as negative control; the experiment and results are shown in Fig. 5b. Based on the ISO standard (ISO document 10 993-5 1992), a hemolysis index of less than 5 % (PMIU-$Ni_{0.25}$: 4.03 %) is considered safe.

Looking into the promising noncytotoxic nature, blood compatibility, self-healing property, tissue-like flexibility (Fig. S10), and 3D printability (Fig. S21) of the hydrogel PMIU-$Ni_{0.25}$, we assessed its potential for wound healing application by using *in vitro* wound healing assay on human keratinocytes (HaCaT). From Fig. 5i and j, significantly faster wound closure happens in the presence of conditioned media compared to control. At the beginning (0 h), around 500 μm of wound distance in both control and PMIU-$Ni_{0.25}$; however, after 12 h, the wound area dramatically reduced in PMIU-$Ni_{0.25}$ system (Fig. 5j2, almost 60 % wound closure) and after 24 h, fully recovery happened (Fig. 5j3). Whereas for control, only 20 % of the wound recovered after 12 h (Fig. 5i2), while 50 % of the wound closed after 24 h (Fig. 5i3). Fast

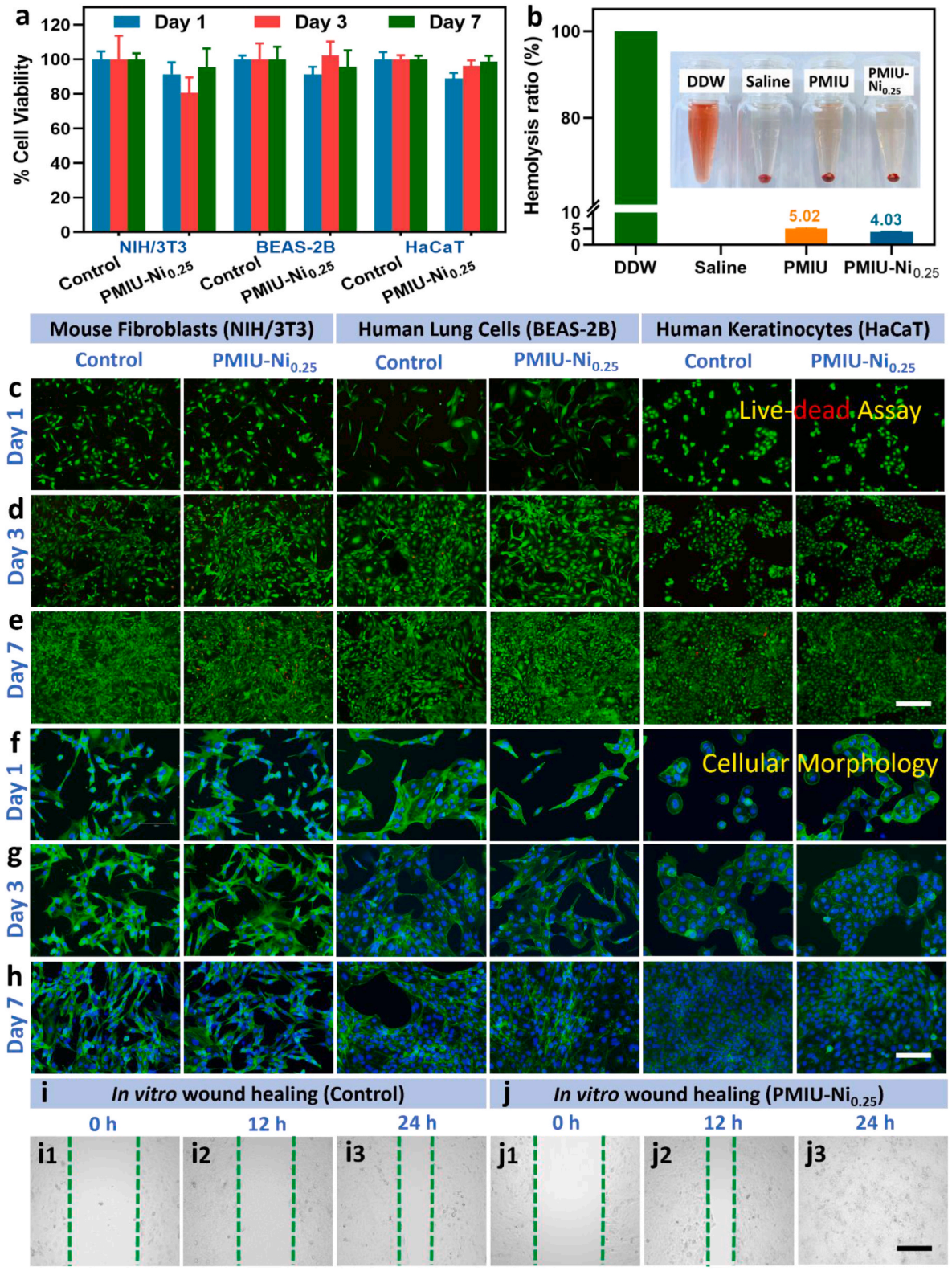

Fig. 5. ***In vitro*** **biocompatibility and** ***in vitro*** **wound healing study.** a) 1-, 3-, and 7-days cell viability of hydrogel PMIU-$Ni_{0.25}$ on three distinct cell lines, NIH/3T3 mouse fibroblasts, BEAS-2B lung epithelial cells, and HaCaT human keratinocytes. b) Blood compatibility of PMIU and PMIU-$Ni_{0.25}$, deionized water as the positive control, and physical saline as the negative control. Live-dead assay of hydrogel PMIU-$Ni_{0.25}$ on NIH/3T3, BEAS-2B, and HaCaT cell lines (scale bar, 300 μm), c) Day 1; d) Day 3; e) Day 7. Cellular morphology of hydrogel PMIU-$Ni_{0.25}$ on NIH/3T3, BEAS-2B, and HaCaT cell lines (scale bar, 150 μm), f) Day 1; g) Day 3; h) Day 7. *In vitro* wound healing assay on HaCat cell line for 24 h (scale bar, 300 μm), i) control; j) PMIU-$Ni_{0.25}$.

wound closure induced by PMIU-$Ni_{0.25}$ suggests it may possess good wound healing capability and be applicable for wound healing applications.

2.5. Antibacterial activity, mechanism and antibiofilm study

Inspired by the excellent mechanical properties, self-healing behavior, and *in vitro* cytocompatibility of synthesized hydrogels, we delved deeper into their antibacterial activity. Given the intrinsic antimicrobial properties of imidazolidinyl urea (Fig. S22) and vinyl imidazole [34,44], we anticipated that our developed hydrogels would exhibit notable efficacy against microbial threats. The antibacterial activity of the polymers PMIU & PMIU-$Ni_{0.25}$ was investigated against Gram-negative *E. coli* and Gram-positive *B. subtilis* using bacterial growth kinetics. The cells were treated with gradient concentrations of PMIU and PMIU-VI supplemented with Ni^{2+} salt (same as formulation of PMIU-$Ni_{0.25}$) for 12 h. The absorbance of untreated and treated bacterial suspensions was periodically measured at 600 nm. Fig. 6a1 and 6b1 present the growth curve of *E. coli* and *B. subtilis* treated with PMIU-$Ni_{0.25}$, clearly indicating that it inhibits both bacteria growth in a concentration-dependent manner. The minimum inhibitory concentrations (MIC) of PMIU-$Ni_{0.25}$ against *E. coli* is 1 mg/mL, and against *B. subtilis* is 0.7 mg/mL. Similar experiments were carried out for PMIU (Figs. S23a and S23b), which show identical MICs of 1 mg/mL and 0.7 mg/mL against *E. coli* and *B. subtilis,* respectively. Further investigations into understanding their bactericidal ability are shown in Fig. 6a2 and 6b2. No bacterial growth at concentrations ≥1 mg/mL for *E. coli* and ≥0.7 mg/mL for *B. subtilis*, revealing that PMIU-$Ni_{0.25}$ could not only inhibit the growth but ultimately kill the microorganisms (MBC). Similarly, for PMIU, no growth is observed on the LB plates at a concentration of 2 mg/mL for *E. coli* and ≥0.7 mg/mL for *B. subtilis* (Figs. S23c and S23d). The results of MIC, MBC, and bactericidal potential of different polymers are summarized in Table S4. The MBC/MIC ratio is widely considered a valuable parameter to evaluate the bactericidal potential of any antibacterial agent. An agent is supposed to be bactericidal if its MBC/MIC ratio is less than or equal to 4. We have observed that for both *E. coli* and *B. subtilis*, the MBC/MIC ratio of the polymers is much less than 4 (Table S4), thereby clearly establishing the bactericidal potential of the polymers.

To clearly understand the origins of developed polymers' antibacterial activities and how these polymers lead to bacterial death, firstly, we conducted an extensive Molecular Dynamics (MD) simulation study (300 ns), focused on the interactions between model bacterial membranes and polymer (oligomer, ESI) in an explicit solvent system. In a meticulously tracked sequence (Fig. 6c and d, S24, and 6e), our investigations unveil that the oligomer's strong propensity to establish close affiliations with and ultimately penetrate the upper membrane leaflet results in substantial alterations in several pivotal dynamic properties. Firstly, the Root Mean Square Deviation (RMSD) analysis discloses a discernible divergence between the RMSD profiles of the upper and lower membrane leaflets (Fig. 6f). This discrepancy was further substantiated by the pronounced RMSD fluctuations of the oligomer, specifically during the MD simulation's 200–275 ns timeframe, effectively corroborating the penetration event (Fig. 6g). Furthermore, the Deuterium Order Parameter analysis provides a keen insight into the differences in the acyl chains of the upper and lower membrane leaflets (Fig. 6h). These differences highlight the significant impact of the oligomer's interaction on the dynamical characteristics of the membrane. Moreover, the 3D surface plots for membrane Area per Lipid (APL) and bilayer thickness (Fig. 6i, j, 6k, and 6l) provide vivid visualizations of the substantial changes in the surface area and thickness of the membrane. This underscores the profound dynamical shifts within the upper membrane leaflet as a direct result of the monomer's interactions.

The comprehensive MD simulation provides a crucial, atomic-level perspective on the intricate dynamics of oligomer-membrane

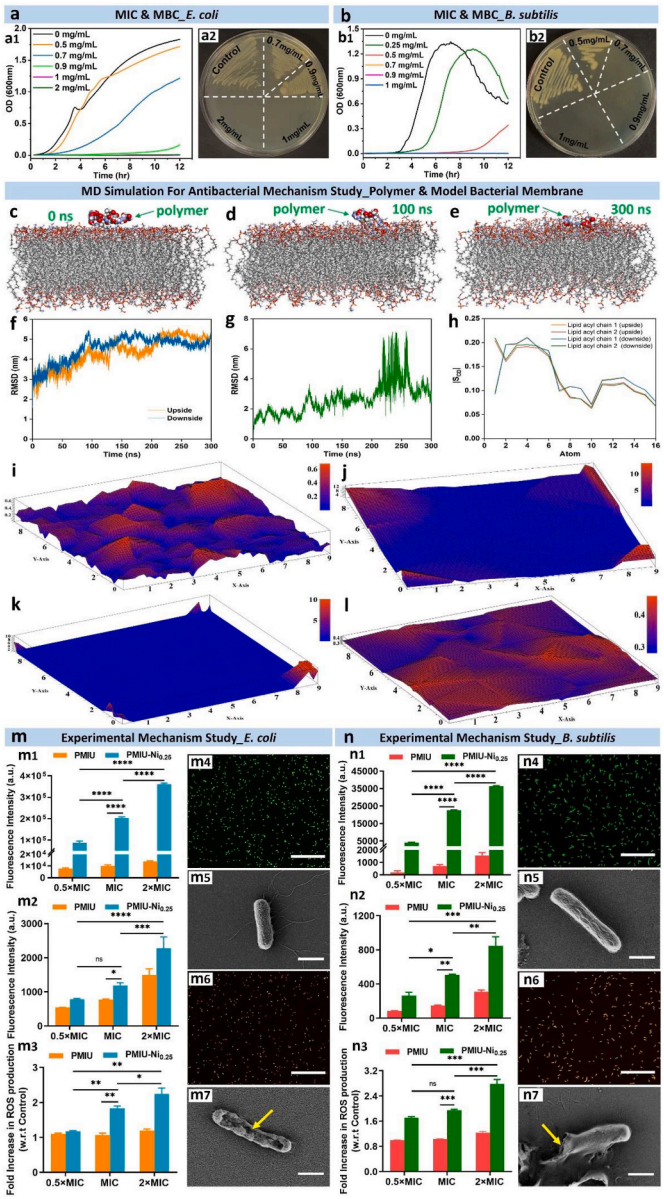

Fig. 6. Antibacterial activity and mechanism of the action of polymers against *E. coli* and *B. subtilis*. a, b) Growth kinetics of bacteria treated with increasing concentrations of PMIU-$Ni_{0.25}$ polymer, a1) *E. coli*; b1) *B. subtilis*. a, b) MBC plate image showing the presence and absence of bacteria growth at different concentrations of PMIU-$Ni_{0.25}$ polymer tested, a2) *E. coli*; b2) *B. subtilis*. Snapshots from MD simulation trajectories at various intervals, c) 0 ns; d) 100 ns; e) 300 ns. f) Root Mean Square Deviation (RMSD) of Gram (−) membrane throughout 300 ns MD simulation. g) Root Mean Square Deviation (RMSD) of oligomer throughout 300 ns MD simulation. h) Deuterium order parameters of the acyl chains presence in Gram (−) membrane. Area per Lipid (APL) surface map (3D) of Gram (−) membrane, i) Upside; j) Downside. Bilayer thickness surface map (3D) of Gram (−) membrane, i) Upside; j) Downside. m, n) Experimental mechanism study of bacteria treated with 0.5 × MIC, MIC, and 2 × MIC of PMIU and PMIU-$Ni_{0.25}$ polymer, cFDA-SE leakage assay, m1) *E. coli*; n1) *B. subtilis*; PI uptake assay, m2) *E. coli*; n2) *B. subtilis*; Intracellular ROS assay, m3) *E. coli*; n3) *B. subtilis*. Live/Dead fluorescence micrograph of untreated and PMIU-$Ni_{0.25}$ polymer-treated bacteria, m4) untreated *E. coli*; m6) treated *E. coli*; n4) untreated *B. subtilis*; n6) treated *B. subtilis*. SEM images of untreated and PMIU-$Ni_{0.25}$ polymer treated bacteria, m5) untreated *E. coli*; m7) treated *E. coli*; n5) untreated *B. subtilis*; n7) treated *B. subtilis*. Scale bar for live-dead images, 75 μm; scale bar for SEM images, 1 μm. Statistical analysis: two-way ANOVA; *, **, ***, and **** were considered for p values < 0.05, <0.01, <0.001, and <0.0001, respectively (n = 3).

interactions, showing the tendency of the active components to bind to and penetrate the bacterial membrane strongly. To further understand this process in greater detail, we next set out to experimentally evaluate the impact of the active components on bacteria and elucidate its mechanism of action. The effect of PMIU and PMIU-$Ni_{0.25}$ on the membrane integrity and morphology of *E. coli* and *B. subtilis* were studied using fluorescent dye-based membrane damage assays. Fig. 6m1 and 6n1 show the results of cFDA-SE leakage assay in *E. coli* and *B. subtilis*, respectively, upon treatment with PMIU and PMIU-$Ni_{0.25}$. 5 (6)-carboxyfluorescein diacetate succinimidyl ester (cFDA-SE) is a membrane permeable dye which is non-fluorescent in its esterified form. Upon entering cells, the intracellular esterases cleave the dye molecules' ester bond, thereby converting them into a fluorescent form [68]. Live bacteria with intact membranes retain the fluorescent dye molecules and appear green. However, cells with damaged or ruptured membranes result in leakage of the dye molecules to the outside, leading to an increase in extracellular fluorescence. Leakage of this fluorescent form of the dye from the bacterial cells is used as a direct parameter to study the membrane integrity of the cells. Treatment of *E. coli* and *B. subtilis* with PMIU and PMIU-$Ni_{0.25}$ resulted in physical disruption of bacterial membrane integrity, as evidenced in the concentration-dependent leakage of cFDA dye molecules from the treated cells. It is observed that the effect of PMIU-$Ni_{0.25}$ on damaging the membrane is more prominent compared to PMIU, which might be due to the combined action of PMIU and Ni ions on bacterial membrane integrity. The membrane damaging potential of PMIU and PMIU-$Ni_{0.25}$ was further confirmed by propidium iodide (PI) uptake assays, as shown in Fig. 6m2 and 6n2. PI can enter cells only if the membrane is damaged or compromised. PI binds to single and double-stranded nucleic acids upon entering cells, producing a strong red fluorescence. Treatment of both *E. coli* and *B. subtilis* with PMIU and PMIU-$Ni_{0.25}$ resulted in a concentration-dependent increase in the uptake of the PI dye molecules by bacteria, as seen from an increase in the PI fluorescence inside the cells. Again, the impact of PMIU-$Ni_{0.25}$ is more significant than PMIU's in damaging bacterial membranes. In addition to membrane damage, we also investigated whether the effect of polymers on bacteria could induce oxidative stress inside the cells, which can also contribute to their antibacterial actions. The levels of total intracellular ROS were measured in untreated and treated cells as an indicator of oxidative stress using the DCFH-DA assay. As seen from Fig. 6m3 and 6n3, treatment of both *E. coli* and *B. subtilis* with PMIU and PMIU-$Ni_{0.25}$ resulted in a concentration-dependent increase in the intracellular ROS levels, with PMIU-$Ni_{0.25}$ contributing towards more oxidative stress generation in comparison to PMIU. A 2.2-fold increase in ROS production concerning control is observed in *E. coli* treated with 2 × MIC of PMIU-$Ni_{0.25}$ compared to treatment with 2 × MIC of PMIU, which induced a 1-fold increase in ROS production. Similarly, a 2.6-fold increase in ROS production is observed in *B. subtilis* upon treatment with 2 × MIC of PMIU-$Ni_{0.25}$ in contrast to a ~0.9-fold increase in ROS production with PMIU. In addition to the polymers, IU also plays a key role in the antibacterial activities, which is a well-known antimicrobial agent, as reported [34,42,69]. The partial hydroxymethyl group of IU could hydrolyze in water, then a trace amount of formaldehyde will be slowly released via dehydration (Fig. S25). The high reducibility of the formyl group could denaturalize the protein of bacterial cells [35]. More specifically, the antimicrobial properties of imidazolidinyl urea compounds are based on their proposed mechanism of protein alkylation of sulfhydryl groups [69,70]. The above studies were further supported by live/dead fluorescence microscopy and SEM images. Untreated *E. coli* (Fig. 6m4) and *B. subtilis* (Fig. 6n4) show uniform green fluorescence, indicating live bacteria, whereas *E. coli* and *B. subtilis* treated with PMIU (Figs. S23e and S23f) and PMIU-$Ni_{0.25}$ (Fig. 6m6 and 6n6) while orange (merge of green and red channel) stain indicating membrane damage and cell death. Similarly, morphological evaluation of bacteria upon treatment with PMIU (Figs. S23g and S23h) and PMIU-$Ni_{0.25}$ (Fig. 6m7 and 6n7) reveal extensive signs of damage and deformation. Untreated cells (Fig. 6m5 and 6n5) show smooth morphology with intact shape, whereas the treated cells appear rough and crumpled with numerous indentations.

After understanding antibacterial mechanisms, the antibacterial activity of PMIU and PMIU-$Ni_{0.25}$ hydrogels against *E. coli* and *B. subtilis* was tested by incubating the cells directly on their surface (Fig. 7a). This process was followed by plating the treated cells on an agar plate to check for the presence or absence of bacterial growth. *E. coli* (Fig. 7b) and *B. subtilis* (Fig. 7d), in the absence of hydrogel, show prominent growth on the agar plates. In contrast, upon direct contact with the hydrogel surface, no colony is observed on the plates, indicating the complete killing of the cells by the hydrogels (Fig. 7c and e, S26a, and S26b). The live/dead fluorescence imaging and SEM results further validate these results. Untreated bacteria (Fig. 7f and h) stain green, showing their viable nature, whereas cells treated with the hydrogel-stained orange represent death (Fig. 7g and i, S26c, and S26d). Similarly, bacteria grown without hydrogel display intact morphology with a smooth appearance (Fig. 7j and l). In contrast, those treated with the hydrogels show damaged and deformed structures, indicating extensive cell death (Fig. 7k and m, S26e, and S26f).

Finally, we evaluated the biofilm inhibition capacity by utilizing both polymer (PMIU-VI supplemented with Ni^{2+} salt (same as formulation of PMIU-$Ni_{0.25}$)) and PMIU-$Ni_{0.25}$ hydrogel. The antibiofilm inhibition study of the polymer was conducted using the well-known crystal violet assay [71] (ESI 1.17) and further supported by brightfield imaging to understand their antibiofilm activity at different concentrations. In detail, the bacterial cells were treated with gradient concentrations (0, 0.5 × MIC, MIC, and 2 × MIC) of polymer and then incubated under static for 48 h to form biofilms. From Fig. 7n and p, both control *E. coli* and *B. subtilis* bacteria form dense biofilms after 2 days, while significant differences are observed in polymers (MIC) treated groups (Fig. 7o and q). Fig. 7r represents the biofilm mass at different polymer concentrations. Almost no biofilm formed at MIC and 2 × MIC in both bacterial groups; even at low concentrations of 0.5 × MIC, significant biofilm mass difference occurred compared to controls. For the hydrogel inhibition study, a small pellet of PMIU-$Ni_{0.25}$ hydrogel was immersed inside the bacteria suspensions, with the same incubation conditions as above for biofilm formation; polymethacrylamide (PMAA) without antibacterial properties as control hydrogel performed same experiments. After 48 h, the biofilm formation on the hydrogel's surface was detected by SEM imaging. As shown in Fig. 7s and u, both *E. coli* and *B. subtilis* bacteria form uniform and dense biofilms on the control PMAA hydrogel surface. In contrast, no bacterium or biofilm is observed on the PMIU-$Ni_{0.25}$ hydrogel surface. Therefore, both polymer and hydrogel inhibition studies strongly indicate their superior antibiofilm activities in preventing biofilm formation in solutions and surfaces. In sum, all the results powerfully demonstrate the antibacterial nature of the designed hydrogels.

3. Conclusions

For the first time, we incorporated the modified IU molecule as the polymers' backbone and successfully synthesized several novel IU-based hydrogels: PMIU, PMIU-Ni_x, and PMIU-Zn_y. Mechanical and rheological studies and hydrogen bonding analysis indicated that introducing dynamic metal-ligand coordination enhances the hydrogel's performance, leading to increased strength and modulus, improved anti-fatigue properties, and more elastic-like behavior. PMIU-$Ni_{0.25}$ hydrogel was identified as the best candidate due to its superior balance of multiple functionalities. Due to the incorporation of multiple H-bonding and dynamic Ni^{2+}/Zn^{2+}-VI coordination, synthesized hydrogels demonstrated rapid self-healing characteristics with high recovery efficiency. These hydrogels could maintain their features between −22 and 70 °C, which is especially appropriate for extreme cold conditions. Rich hydrogen bonds between water molecules and polymer structures will significantly enhance the moisture-holding capability, and the

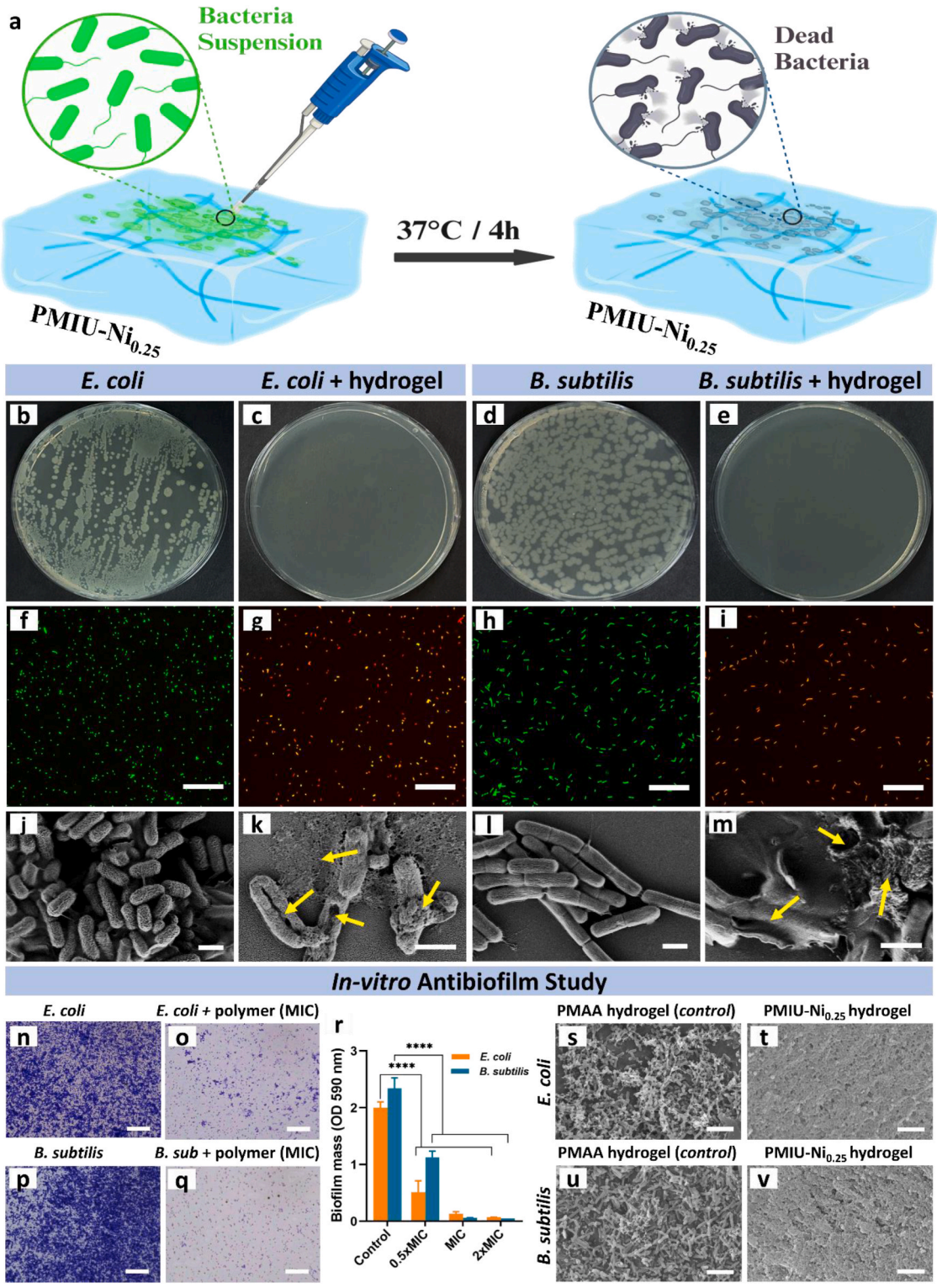

Fig. 7. Antibacterial and antibiofilm study of hydrogel PMIU-Ni$_{0.25}$. a) Schematic illustration of the antibacterial study process. Colony formation assay, b) untreated *E. coli*; c) *E. coli* on hydrogel; d) untreated *B. subtilis*; e) *B. subtilis* on hydrogel. Live-dead assay, scale bar 75 μm, f) untreated *E. coli*; g) *E. coli* on hydrogel; h) untreated *B. subtilis*; i) *B. subtilis* on hydrogel. SEM morphology, scale bar 1 μm, j) untreated *E. coli*; k) *E. coli* on hydrogel; l) untreated *B. subtilis*; m) *B. subtilis* on hydrogel. Crystal violet (CV) assay to study biofilm inhibition at gradient PMIU-VI polymer supplemented with Ni^{2+} salt (same as formulation of PMIU-Ni$_{0.25}$) concentrations, scale bar 75 μm, n) control *E. coli* biofilm stained by CV; o) polymer (MIC) treated *E. coli* stained by CV; p) control *B. subtilis* biofilm stained by CV; q) polymer (MIC) treated *B. subtilis* stained by CV; r) biofilm mass of different concentrations polymer treated samples compared to controls. Antibiofilm study on hydrogels by SEM, scale bar 5 μm, s) *E. coli* biofilm on control hydrogel PMAA; t) *E. coli* on hydrogel PMIU-Ni$_{0.25}$, no biofilm; u) *B. subtilis* biofilm on control hydrogel PMAA; v) *B. subtilis* on hydrogel PMIU-Ni$_{0.25}$, no biofilm. Statistical analysis: two-way ANOVA; *, **, ***, and **** were considered for p values < 0.05, <0.01, <0.001, and <0.0001, respectively ($n = 3$).

introduction of hydrophobic moieties (methyl groups) and urea structures could lower the freezing point, in which the hydrophobic aggregates confined the growth of ice nuclei to proceed with crystallization.

Furthermore, *in vitro* biocompatibility evaluation showed no significant cytotoxic effects of PMIU-$Ni_{0.25}$ against three distinct cell lines NIH/3T3 mouse fibroblasts, BEAS-2B human lung epithelial cells, and HaCaT human keratinocytes, as well as good hemocompatibility against human blood cells. In addition, an *in vitro* wound healing study proved that PMIU-$Ni_{0.25}$ could potentially promote wound healing. Moreover, polymers and hydrogels of PMIU and PMIU-$Ni_{0.25}$ exhibited excellent antibacterial activity against gram-negative *E. coli* and gram-positive *B. subtilis*. Intrinsic mechanism study involved extensive MD simulation of polymer-model bacterial membrane interactions and fluorescence-based experimental assays. The comprehensive MD simulation provided a crucial, atomic-level perspective on the intricate dynamics of oligomer-membrane interactions, showing the tendency of the active components to bind to and penetrate the bacterial membrane strongly. Further, experimental assays indicated that the polymers could penetrate and damage the bacterial membrane, and the induction of oxidative stress by concentration-dependent reactive oxygen species (ROS) generation will cause intracellular oxidative damage. Finally, the biofilm inhibition study of both polymer and hydrogel strongly indicated their superior antibiofilm activities, to prevent the biofilm formation in solutions and surfaces. In sum, all results strongly demonstrate the attractive material features and antibacterial nature of the designed hydrogels, which provide various potentials for infectious wound care, such as treating wound infections and promoting wound healing. Meanwhile, the 3D-printability of these hydrogels opens their promising applications in the future as carriers and scaffolds for drug delivery and tissue engineering. For example, as a drugs-loading antibiofilm dressing material, treating multi-drug-resistant bacterial infected wounds.

4. Experimental section

All details of materials, preparations, characterizations, study methods, and extra data were shown in supporting information.

Ethics approval and consent to participate

Blood Compatibility Study.

Blood samples were purchased from the Magen David Adom Blood Bank, and the blood compatibility study was approved by the Institutional Review Board and Human Subject Protection Committee of Technion-Israel Institute of Technology, approval number 189–2024.

CRediT authorship contribution statement

Qi Wu: Writing – review & editing, Writing – original draft, Validation, Software, Project administration, Methodology, Investigation, Formal analysis, Data curation, Conceptualization. **Krishanu Ghosal:** Writing – review & editing, Methodology, Investigation. **Nadine Kana'an:** Writing – review & editing, Investigation. **Shounak Roy:** Writing – review & editing, Investigation. **Nagham Rashed:** Investigation. **Ranabir Majumder:** Writing – review & editing, Software. **Mahitosh Mandal:** Software. **Liang Gao:** Software. **Shady Farah:** Supervision.

Declaration of competing interest

The authors declare that they have no known competing financial interests or personal relationships that could have appeared to influence the work reported in this paper.

Acknowledgment

The Neubauer Family Foundation is thanked for their generous funding and support. S.F. was supported by MAOF Fellowship from the Council for Higher Education, Israel. K.G. acknowledges Aly Kaufman Fellowship Trust for partial support of his fellowship. This work was also partially supported by the Israel Science Foundation and the Technion's president grant, and we thank them for that.

The DFT calculation and MD simulation of H-bonding analysis parts collaborated with Jinan Key Laboratory of High Performance Industrial Software, Jinan Institute of Supercomputing Technology, China. The MD simulation for bacterial mechanism analysis part collaborated with School of Medical Science and Technology, Indian Institute of Technology Kharagpur, West Bengal, India. We highly appreciate and thank them for their efforts. R.M. and M.M. gratefully acknowledge use of the "PARAM Shakti" supercomputer, provided under the National Supercomputing Mission and supported by the Government of India, located at the Indian Institute of Technology Kharagpur". They also acknowledge financial support from the Science and Engineering Research Board (SERB), Department of Science and Technology, Government of India, under grant number JCB/2019/000008.

Appendix A. Supplementary data

Supplementary data to this article can be found online at https://doi.org/10.1016/j.bioactmat.2024.10.003.

References

[1] T.R. Walsh, A.C. Gales, R. Laxminarayan, P.C. Dodd, Antimicrobial resistance: addressing a global threat to humanity, PLoS Med. 20 (7) (2023) e1004264.
[2] R.M. Klevens, J.R. Edwards, C.L. Richards, T.C. Horan, R.P. Gaynes, D.A. Pollock, D.M. Cardo, Estimating health care-associated infections and deaths in U.S. Hospitals, Publ. Health Rep. 122 (2) (2002) 160–166, 2007.
[3] C.G. Starr, J. Ghimire, S. Guha, J.P. Hoffmann, Y. Wang, L. Sun, B.N. Landreneau, Z.D. Kolansky, I.M. Kilanowski-Doroh, M.C. Sammarco, L.A. Morici, W.C. Wimley, Synthetic molecular evolution of host cell-compatible, antimicrobial peptides effective against drug-resistant, biofilm-forming bacteria, Proc. Natl. Acad. Sci. USA 117 (15) (2020) 8437–8448.
[4] C. He, C. Liu, M. Li, M. Li, J. Yin, S. Han, J. Xia, D. Chen, W. Cao, Q. Lu, F. Rosei, 3D hierarchical Cu-MOF nanosheets-based antibacterial mesh, Chem. Eng. J. 446 (2022) 137381.
[5] Z. Wang, X. Liu, Y. Duan, Y. Huang, Infection microenvironment-related antibacterial nanotherapeutic strategies, Biomaterials 280 (2022) 121249.
[6] M. Wang, X. Huang, H. Zheng, Y. Tang, K. Zeng, L. Shao, L. Li, Nanomaterials applied in wound healing: mechanisms, limitations and perspectives, J. Contr. Release 337 (2021) 236–247.
[7] S.K. Nethi, S. Das, C.R. Patra, S. Mukherjee, Recent advances in inorganic nanomaterials for wound-healing applications, Biomater. Sci. 7 (7) (2019) 2652–2674.
[8] K. Schuhladen, P. Mukoo, L. Liverani, Z. Neščáková, A.R. Boccaccini, Manuka honey and bioactive glass impart methylcellulose foams with antibacterial effects for wound-healing applications, Biomed. Mater. 15 (6) (2020) 065002.
[9] A. Gefen, P. Alves, D. Beeckman, J.L. Lázaro-Martínez, H. Lev-Tov, B. Najafi, T. Swanson, K. Woo, Mechanical and contact characteristics of foam materials within wound dressings: theoretical and practical considerations in treatment, Int. Wound J. 20 (6) (2023) 1960–1978.
[10] A. Memic, T. Abdullah, H.S. Mohammed, K. Joshi Navare, T. Colombani, S. A. Bencherif, Latest progress in electrospun nanofibers for wound healing applications, ACS Appl. Bio Mater. 2 (3) (2019) 952–969.
[11] C. Cui, S. Sun, S. Wu, S. Chen, J. Ma, F. Zhou, Electrospun chitosan nanofibers for wound healing application, Eng. Regener. 2 (2021) 82–90.
[12] A. Farazin, F.A. Shirazi, M. Shafiei, Natural biomarocmolecule-based antimicrobial hydrogel for rapid wound healing: a review, Int. J. Biol. Macromol. 244 (2023) 125454.
[13] W. Wang, S. Ummartyotin, R. Narain, Advances and challenges on hydrogels for wound dressing, Curre. Opini. Biomed. Eng. 26 (2023) 100443.
[14] M.H. Norahan, S.C. Pedroza-González, M.G. Sánchez-Salazar, M.M. Álvarez, G. Trujillo de Santiago, Structural and biological engineering of 3D hydrogels for wound healing, Bioact. Mater. 24 (2023) 197–235.
[15] Q. Wu, E. Nassar-Marjiya, M. Elias, S. Farah, Fundamentals and biomedical applications of smart hydrogels, Biomateri. Biopoly. (2023) 71–93. Springer.
[16] K. Ghosal, D. Chakraborty, V. Roychowdhury, S. Ghosh, S. Dutta, Recent advancement of functional hydrogels toward diabetic wound management, ACS Omega 7 (48) (2022) 43364–43380.
[17] J. Li, Y. Wang, J. Yang, W. Liu, Bacteria activated-macrophage membrane-coated tough nanocomposite hydrogel with targeted photothermal antibacterial ability for infected wound healing, Chem. Eng. J. 420 (2021) 127638.
[18] L. Mao, L. Wang, M. Zhang, M.W. Ullah, L. Liu, W. Zhao, Y. Li, A.A.Q. Ahmed, H. Cheng, Z. Shi, G. Yang, In situ synthesized selenium nanoparticles-decorated bacterial cellulose/gelatin hydrogel with enhanced antibacterial, antioxidant, and

anti-inflammatory capabilities for facilitating skin wound healing, Adv. Healthcare Mater. 10 (14) (2021) 2100402.
[19] J. Li, J. Ma, H. Sun, M. Yu, H. Wang, Q. Meng, Z. Li, D. Liu, J. Bai, G. Liu, X. Xing, F. Han, B. Li, Transformation of arginine into zero-dimensional nanomaterial endows the material with antibacterial and osteoinductive activity, Sci. Adv. 9 (21) (2023) eadf8645.
[20] H. Qiu, Z. Si, Y. Luo, P. Feng, X. Wu, W. Hou, Y. Zhu, M.B. Chan-Park, L. Xu, D. Huang, The Mechanisms and the Applications of Antibacterial Polymers in Surface Modification on Medical Devices, vol. 8, 2020, p. 910.
[21] W. Chin, C. Yang, V.W.L. Ng, Y. Huang, J. Cheng, Y.W. Tong, D.J. Coady, W. Fan, J. L. Hedrick, Y.Y. Yang, Biodegradable broad-spectrum antimicrobial polycarbonates: investigating the role of chemical structure on activity and selectivity, Macromolecules 46 (22) (2013) 8797–8807.
[22] J. Hoque, R.G. Prakash, K. Paramanandham, B.R. Shome, J. Haldar, Biocompatible injectable hydrogel with potent wound healing and antibacterial properties, Mol. Pharm. 14 (4) (2017) 1218–1230.
[23] M. Bisharat, K. Ghosal, N. Kana'an, B. Khamaisi, E. Nassar-Marjiya, S. Jindal, S. Farah, Engineering fully quaternized (Dimethylamino)ethyl methacrylate-based photoresins for 3D printing of biodegradable antimicrobial polymers, Chem. Eng. J. (2024) 155417.
[24] L.L. Ling, T. Schneider, A.J. Peoples, A.L. Spoering, I. Engels, B.P. Conlon, A. Mueller, T.F. Schäberle, D.E. Hughes, S. Epstein, M. Jones, L. Lazarides, V. A. Steadman, D.R. Cohen, C.R. Felix, K.A. Fetterman, W.P. Millett, A.G. Nitti, A. M. Zullo, C. Chen, K. Lewis, A new antibiotic kills pathogens without detectable resistance, Nature 517 (7535) (2015) 455–459.
[25] L. Liu, H. Wu, S.N. Riduan, J.Y. Ying, Y. Zhang, Short imidazolium chains effectively clear fungal biofilm in keratitis treatment, Biomaterials 34 (4) (2013) 1018–1023.
[26] W. Chin, G. Zhong, Q. Pu, C. Yang, W. Lou, P.F. De Sessions, B. Periaswamy, A. Lee, Z.C. Liang, X. Ding, S. Gao, C.W. Chu, S. Bianco, C. Bao, Y.W. Tong, W. Fan, M. Wu, J.L. Hedrick, Y.Y. Yang, A macromolecular approach to eradicate multidrug resistant bacterial infections while mitigating drug resistance onset, Nat. Commun. 9 (1) (2018) 917.
[27] K. Chindera, M. Mahato, A. Kumar Sharma, H. Horsley, K. Kloc-Muniak, N. F. Kamaruzzaman, S. Kumar, A. McFarlane, J. Stach, T. Bentin, L. Good, The antimicrobial polymer PHMB enters cells and selectively condenses bacterial chromosomes, Sci. Rep. 6 (1) (2016) 23121.
[28] P.E. Beaumont, B. McHugh, E. Gwyer Findlay, A. Mackellar, K.J. Mackenzie, R. L. Gallo, J.R.W. Govan, A.J. Simpson, D.J. Davidson, Cathelicidin host defence peptide augments clearance of pulmonary Pseudomonas aeruginosa infection by its influence on neutrophil function in vivo, PLoS One 9 (6) (2014) e99029.
[29] N. Mookherjee, M.A. Anderson, H.P. Haagsman, D.J. Davidson, Antimicrobial host defence peptides: functions and clinical potential, Nat. Rev. Drug Discov. 19 (5) (2020) 311–332.
[30] A.K. Ghosh, M. Brindisi, Urea derivatives in modern drug discovery and medicinal chemistry, J. Med. Chem. 63 (6) (2020) 2751–2788.
[31] P. Claudon, A. Violette, K. Lamour, M. Decossas, S. Fournel, B. Heurtault, J. Godet, Y. Mély, B. Jamart-Grégoire, M.-C. Averlant-Petit, J.-P. Briand, G. Duportail, H. Monteil, G. Guichard, Consequences of isostructural main-chain modifications for the design of antimicrobial foldamers: helical mimics of host-defense peptides based on a heterogeneous amide/urea backbone, Angew. Chem. Int. Ed. 49 (2) (2010) 333–336.
[32] O. Ommi, M. Naiyaz Ahmad, S.N.R. Gajula, P. Wanjari, S. Sau, P.K. Agnivesh, S. K. Sahoo, N.P. Kalia, R. Sonti, S. Nanduri, A. Dasgupta, S. Chopra, V. M. Yaddanapudi, Synthesis and pharmacological evaluation of 1,3-diaryl substituted pyrazole based (thio)urea derivatives as potent antimicrobial agents against multi-drug resistant Staphylococcus aureus and Mycobacterium tuberculosis, RSC Med. Chem. 14 (7) (2023) 1296–1308.
[33] J. Cortez Karoll, E. Roilides, F. Quiroz-Telles, J. Meletiadis, C. Antachopoulos, T. Knudsen, W. Buchanan, J. Milanovich, A. Sutton Deanna, A. Fothergill, G. Rinaldi Michael, R. Shea Yvonne, T. Zaoutis, S. Kottilil, J. Walsh Thomas, Infections caused by scedosporium spp, Clin. Microbiol. Rev. 21 (1) (2008) 157–197.
[34] S.V. Lehmann, U. Hoeck, J. Breinholdt, C.E. Olsen, B. Kreilgaard, Characterization and chemistry of imidazolidinyl urea and diazolidinyl urea, Contact Dermatitis 54 (1) (2006) 50–58.
[35] J. Xu, Z. Wang, L. Yu, J. Wang, S. Wang, A novel reverse osmosis membrane with regenerable anti-biofouling and chlorine resistant properties, J. Membr. Sci. 435 (2013) 80–91.
[36] J. Yu, X. Chen, Y. Yang, X. Zhao, X. Chen, T. Jing, Y. Zhou, J. Xu, Y. Zhang, Y. Cheng, Construction of supramolecular hydrogels using imidazolidinyl urea as hydrogen bonding reinforced factor, J. Mater. Chem. B 8 (15) (2020) 3058–3063.
[37] Y. Yang, X. Zhao, J. Yu, X. Chen, X. Chen, C. Cui, J. Zhang, Q. Zhang, Y. Zhang, S. Wang, Y. Cheng, H-bonding supramolecular hydrogels with promising mechanical strength and shape memory properties for postoperative antiadhesion application, ACS Appl. Mater. Interfaces 12 (30) (2020) 34161–34169.
[38] Q. Zhong, X. Chen, Y. Yang, C. Cui, L. Ma, Z. Li, Q. Zhang, X. Chen, Y. Cheng, Y. Zhang, Hydrogen bond reinforced, transparent polycaprolactone-based degradable polyurethane, Mater. Chem. Front. 5 (14) (2021) 5371–5381.
[39] R. Wang, X. Chen, Y. Yang, Y. Xu, Q. Zhang, Y. Zhang, Y. Cheng, Imidazolidinyl urea reinforced polyacrylamide hydrogels through the formation of multiple hydrogen bonds, React. Funct. Polym. 172 (2022) 105183.
[40] Y. Yang, X. Zhao, S. Wang, Y. Zhang, A. Yang, Y. Cheng, X. Chen, Ultra-durable cell-free bioactive hydrogel with fast shape memory and on-demand drug release for cartilage regeneration, Nat. Commun. 14 (1) (2023) 7771.
[41] Y. Yang, X. Zhao, J. Yu, X. Chen, R. Wang, M. Zhang, Q. Zhang, Y. Zhang, S. Wang, Y. Cheng, Bioactive skin-mimicking hydrogel band-aids for diabetic wound healing and infectious skin incision treatment, Bioact. Mater. 6 (11) (2021) 3962–3975.
[42] N. Rashed, K. Ghosal, N. Kana'an, Q. Wu, K. Reddy Kunduru, S. Farah, Engineering multifunctional UV-polymerizable imidazolidinyl urea-based methacrylate resin for 3D printing: synthesis, characterization, and antimicrobial properties, Chem. Eng. J. 488 (2024) 150737.
[43] S. Lin, X. Liu, J. Liu, H. Yuk, H.-C. Loh, G.A. Parada, C. Settens, J. Song, A. Masic, G.H. McKinley, X. Zhao, Anti-fatigue-fracture hydrogels, Sci. Adv. 5 (1) (2019) eaau8528.
[44] L. Zhang, X.-M. Peng, G.L.V. Damu, R.-X. Geng, C.-H. Zhou, Comprehensive review in current developments of imidazole-based medicinal chemistry, Med. Res. Rev. 34 (2) (2014) 340–437.
[45] X.-K. Jin, J.-L. Liang, S.-M. Zhang, P. Ji, Q.-X. Huang, Y.-T. Qin, X.-C. Deng, C.-J. Liu, X.-Z. Zhang, Engineering metal-based hydrogel-mediated tertiary lymphoid structure formation via activation of the STING pathway for enhanced immunotherapy, Mater. Horiz. 10 (10) (2023) 4365–4379.
[46] A. Dutta, K. Ghosal, K. Sarkar, D. Pradhan, R.K. Das, From ultrastiff to soft materials: exploiting dynamic metal–ligand cross-links to access polymer hydrogels combining customized mechanical performance and tailorable functions by controlling hydrogel mechanics, Chem. Eng. J. 419 (2021) 129528.
[47] C.-H. Li, J.-L. Zuo, Self-healing polymers based on coordination bonds, Adv. Mater. 32 (27) (2020) 1903762.
[48] E. Khare, N. Holten-Andersen, M.J. Buehler, Transition-metal coordinate bonds for bioinspired macromolecules with tunable mechanical properties, Nat. Rev. Mater. 6 (5) (2021) 421–436.
[49] R. Bai, J. Yang, Z. Suo, Fatigue of hydrogels, Eur. J. Mech. Solid. 74 (2019) 337–370.
[50] C. Xiang, Z. Wang, C. Yang, X. Yao, Y. Wang, Z. Suo, Stretchable and fatigue-resistant materials, Mater. Today 34 (2020) 7–16.
[51] K. Cui, Y.N. Ye, C. Yu, X. Li, T. Kurokawa, J.P. Gong, Stress relaxation and underlying structure evolution in tough and self-healing hydrogels, ACS Macro Lett. 9 (11) (2020) 1582–1589.
[52] K. Cui, Y.N. Ye, T.L. Sun, C. Yu, X. Li, T. Kurokawa, J.P. Gong, Phase separation behavior in tough and self-healing polyampholyte hydrogels, Macromolecules 53 (13) (2020) 5116–5126.
[53] N.R. Richbourg, M. Wancura, A.E. Gilchrist, S. Toubbeh, B.A.C. Harley, E. Cosgriff-Hernandez, N.A. Peppas, Precise control of synthetic hydrogel network structure via linear, independent synthesis-swelling relationships, Sci. Adv. 7 (7) (2021) eabe3245.
[54] K. Zhang, Q. Feng, Z. Fang, L. Gu, L. Bian, Structurally dynamic hydrogels for biomedical applications: pursuing a fine balance between macroscopic stability and microscopic dynamics, Chem. Rev. 121 (18) (2021) 11149–11193.
[55] Y. Hirashima, H. Sato, A. Suzuki, ATR-FTIR spectroscopic study on hydrogen bonding of poly(N-isopropylacrylamide-co-sodium acrylate) gel, Macromolecules 38 (22) (2005) 9280–9286.
[56] S. Wu, T.-W. Wang, Y. Du, B. Yao, S. Duan, Y. Yan, M. Hua, Y. Alsaid, X. Zhu, X. He, Tough, anti-freezing and conductive ionic hydrogels, NPG Asia Mater. 14 (1) (2022) 65.
[57] Y. Xu, Q. Rong, T. Zhao, M. Liu, Anti-Freezing multiphase gel materials: bioinspired design strategies and applications, Giant 2 (2020) 100014.
[58] C.G. Wiener, M. Tyagi, Y. Liu, R.A. Weiss, B.D. Vogt, Supramolecular hydrophobic aggregates in hydrogels partially inhibit ice formation, J. Phys. Chem. B 120 (24) (2016) 5543–5552.
[59] K. Liu, C. Wang, J. Ma, G. Shi, X. Yao, H. Fang, Y. Song, J. Wang, Janus effect of antifreeze proteins on ice nucleation, Proc. Natl. Acad. Sci. USA 113 (51) (2016) 14739–14744.
[60] X.P. Morelle, W.R. Illeperuma, K. Tian, R. Bai, Z. Suo, J.J. Vlassak, Highly stretchable and tough hydrogels below water freezing temperature, Adv. Mater. 30 (35) (2018) 1801541.
[61] C. Wang, C.G. Wiener, P.I. Sepulveda-Medina, C. Ye, D.S. Simmons, R. Li, M. Fukuto, R.A. Weiss, B.D. Vogt, Antifreeze hydrogels from amphiphilic statistical copolymers, Chem. Mater. 31 (1) (2019) 135–145.
[62] G. Stojkov, Z. Niyazov, F. Picchioni, R.K. Bose, Relationship between structure and rheology of hydrogels for various applications, Gels 7 (4) (2021) 255.
[63] K. Hyun, M. Wilhelm, C.O. Klein, K.S. Cho, J.G. Nam, K.H. Ahn, S.J. Lee, R. H. Ewoldt, G.H. McKinley, A review of nonlinear oscillatory shear tests: analysis and application of large amplitude oscillatory shear (Laos), Prog. Polym. Sci. 36 (12) (2011) 1697–1753.
[64] M.E. Allen, J.W. Hindley, D.K. Baxani, O. Ces, Y. Elani, Hydrogels as functional components in artificial cell systems, Nat. Rev. Chem 6 (8) (2022) 562–578.
[65] H. Rammal, A. GhavamiNejad, A. Erdem, R. Mbeleck, M. Nematollahi, S. Emir Diltemiz, H. Alem, M.A. Darabi, Y.N. Ertas, E.J. Caterson, N. Ashammakhi, Advances in biomedical applications of self-healing hydrogels, Mater. Chem. Front. 5 (12) (2021) 4368–4400.
[66] N. Kutner, K.R. Kunduru, L. Rizik, S. Farah, Recent advances for improving functionality, biocompatibility, and longevity of implantable medical devices and deliverable drug delivery systems, Adv. Funct. Mater. 31 (44) (2021) 2010929.
[67] S. Jindal, K. Ghosal, B. Khamaisi, N. Kana'an, E. Nassar-Marjiya, S. Farah, Facile green synthesis of zingerone based tissue-like biodegradable polyester with shape-memory features for regenerative medicine, Adv. Funct. Mater. (2024) 2405827.
[68] S. Roy, A. Mondal, V. Yadav, A. Sarkar, R. Banerjee, P. Sanpui, A. Jaiswal, Mechanistic insight into the antibacterial activity of chitosan exfoliated MoS2 nanosheets: membrane damage, metabolic inactivation, and oxidative stress, ACS Appl. Bio Mater. 2 (7) (2019) 2738–2755.

[69] C.M. Llabres, D. Ahearn, Antimicrobial activities of N-chloramines and diazolidinyl urea, Appl. Environ. Microbiol. 49 (2) (1985) 370–373.
[70] I. Dahlquist, S. Fregert, Formaldehyde releasers, Contact Dermatitis 4 (3) (1978).
[71] J. Zhou, J. Mei, Q. Liu, D. Xu, X. Wang, X. Zhang, W. Zhu, C. Zhu, J. Wang, Spatiotemporal on–off immunomodulatory hydrogel targeting NLRP3 inflammasome for the treatment of biofilm-infected diabetic wounds, Adv. Funct. Mater. 33 (12) (2023) 2211811.